The Astrophysical Journal, 899:108 (10pp), 2020 August 20 https://doi.org/10.3847/1538-4357/aba26f

Massive Galaxies Impede Massive Outflows

Ryan Tanner[1,2]
[1] NASA Goddard Space Flight Center, Greenbelt, MD 20771, USA; ryan.tanner@nasa.gov
[2] Augusta University, Augusta, GA 30912, USA
Received 2020 May 13; revised 2020 June 24; accepted 2020 July 1; published 2020 August 18

Abstract

A set of 66 3D hydrodynamical simulations explores how galactic stellar mass affects three-phase, starburst-driven outflows. Simulated velocities are compared to two basic analytic models: with and without a gravitational potential. For stellar mass $<10^{10} M_{\odot}$, simulated velocities match those of both analytical models and are unaffected by the potential; above they reduce significantly as expected from the analytic model with gravity. Gravity also affects total outflow mass and each of the three phases differently. Outflow masses in the hot, warm, and cold phases each scale with stellar mass as $\log M_{*} = -0.25$, -0.97, and -1.70, respectively. Thus, the commonly used Chevalier & Clegg analytic model should be modified to include gravity when applied to higher-mass galaxies. In particular, using M82 as the canonical galaxy to interpret hydrodynamical simulations of starburst-driven outflows from higher-mass galaxies will underestimate the retarding effect of gravity. Using the analytic model of Johnson & Axford with realistic thermalization efficiency and mass loading, I find that only galaxy masses $\lesssim 10^{11.5} M_{\odot}$ can outflow.

Unified Astronomy Thesaurus concepts: Starburst galaxies (1570); Active galaxies (17); Galactic winds (572); Galaxy winds (626); Hydrodynamical simulations (767); Scaling relations (2031); Galaxy properties (615); Galaxy kinematics (602); Galaxy processes (614)

1. Introduction

Much observational and modeling work has established scaling relations between host galaxy properties and the kinematics and content of galactic "superwind" outflows (Veilleux et al. 2005, 2020; Heckman & Thompson 2017; Rupke 2018; Zhang et al. 2018). Influential host galaxy properties include star formation rate (SFR), SFR density, UV, optical, and IR emission and absorption, galaxy mass, thermalization efficiency, and mass loading.

A still popular galactic outflow model was proposed by Chevalier & Clegg (1985, hereafter CC85) with wind generated by thermal overpressure of a nuclear starburst (Veilleux et al. 2005; Heckman & Thompson 2017). CC85 argued that gravity barely affects the outflow. Subsequent wind models added radiation pressure (Nath & Silk 2009; Thompson et al. 2015) or cosmic rays (Ipavich 1975; Hopkins et al. 2020), or all three (Yu et al. 2020), to improve upon CC85. The less employed Johnson & Axford (1971, hereafter JA71) model also uses thermal overpressure to generate a wind but adds a spherical gravitational potential.

Variants of the CC85 model have determined the inputs and subgrid parameters of galactic-scale hydrodynamical simulations (Strickland & Stevens 2000; Cooper et al. 2008; Tanner et al. 2017 (hereafter Tanner17); Schneider et al. 2020; Yu et al. 2020). Yu et al. 2020 review how the models affect the mass-loading rates, mass and energy outflow rates, and terminal wind velocities by following several gas phases (Lehnert et al. 1999; Veilleux et al. 2009; McCormick et al. 2013). But as Schneider et al. (2020) show, different CC85 model variants can influence differently each phase of a galactic outflow.

Different motions of each phase arising from differing determining factors require that we treat each separately (Heckman & Borthakur 2016; Martin et al. 2019; Schneider et al. 2020). In Tanner17 I discussed my 3D simulations that reproduced and explained some of the observed scaling relations between galactic wind velocities and the SFR. In this paper I use my simulations to compare the predictions of the basic CC85 model to that of the JA71 model over a range of galaxy mass. Section 2 explains my setup, and carefully defines the term mass loading because it is used differently by different authors. I then explain how I measure the velocities of the three-phase outflow, and in Section 3 show how they are better explained by the JA71 model. In Section 4 I show how my simulations reproduce the observed negative correlation between mass outflow rate and galaxy mass. In Section 5 I explore the consequences of the JA71 model versus the CC85 model on the predicted maximum galaxy mass at which galactic outflows can form.

2. Simulation Setup

To explore how outflow velocities scale with galaxy mass I set up a series of hydro-simulations using the Athena (Stone et al. 2008) magnetohydrodynamic code with magnetic fields turned off. The canonical model is an M82-mass galaxy (Cooper et al. 2008; Tanner17). I model its disk by adding a Plummer–Kuzmin potential (Miyamoto & Nagai 1975)

$$\Phi_{\rm disk}(r, z) = -\frac{GM_{\rm disk}}{\sqrt{r^2 + (a + \sqrt{z^2 + b^2})^2}} \quad (1)$$

to a spherical King model

$$\Phi_{\rm ss}(R) = -\frac{GM_{\rm ss}}{r_0}\left[\frac{\ln[(R/r_0) + \sqrt{1 + (R/r_0)^2}\,]}{(R/r_0)}\right]. \quad (2)$$

Galaxy parameters for the potentials are the same as in Tanner17, except that I vary the stellar $M_{\rm disk}$ from $10^{9.6} M_{\odot}$ to $10^{10.6} M_{\odot}$ in steps of 0.2 dex. I did not include a dark matter halo; when I included one in my analytic models it

did not change any of the relations or conclusions presented in this paper. But for completeness a dark matter halo should be included in all future simulations. The thickness of the gaseous disk is set by a tanh profile of scale height 110 pc to correct the nonphysical flaring of the disk at large radii as seen in Cooper et al. (2008) and Tanner17. For each galaxy mass I run 11 simulations with CC85 model velocities ranging from 400 to 2400 km s^{-1} in steps of 200 km s^{-1}, 66 simulations in all. I choose the CC85 model velocity and set the thermalization efficiency (ϵ) to 1.0, then calculate mass loading (β) using Equation (7). The initial gas density distribution is set by a semi-random fractal distribution as in Tanner17. Within the starburst region, mass and energy are injected proportional to the initial density, with total energy and mass injection rates set by a Starburst99 model with an SFR of 50 $M_\odot$ yr^{-1}.

2.1. Thermalization Efficiency and Mass Loading

Thermalization efficiency (ϵ), the fraction 0 to 1 of starburst power output absorbed by the surrounding medium, varies with environment and perhaps time (Freyer et al. 2003; Veilleux et al. 2005; Silich et al. 2009; Strickland & Heckman 2009; Kim & Ostriker 2015). Freyer et al. (2003) estimated that immediately after star formation $\epsilon \approx 0.1$ but would thereafter fall quickly to ≈0.01. Silich et al. (2009) measured $\epsilon < 0.1$ for star clusters in M82, but Strickland & Heckman (2009) modeled a range of 0.1–1.0 finding >0.3 most likely in M82. Kim & Ostriker (2015) found that ϵ could shift rapidly between 1 and 0.1–0.3 depending on environmental and starburst properties. Here I set $\epsilon = 1.0$.

The term mass loading is easily confused because it is used in different papers to refer to related but different things. CC85 used it to refer to all gas swept up from a star cluster, including mass from stellar winds, supernova ejecta, gas left over from star formation, and any diffuse ambient interstellar medium (ISM). In their formulation, mass loading would be

$$\dot{M} = \dot{M}_{\rm SN+SW} + \dot{M}_{\rm cold} + \dot{M}_{\rm ISM}. \quad (3)$$

Simulations of nuclear starbursts use a sub-grid model to account for sub-parsec-scale gas remaining from star formation (Strickland & Stevens 2000; Cooper et al. 2008; Strickland & Heckman 2009; Tanner17). Mass injected by stellar winds and supernovae ($\dot{M}_{\rm SN+SW}$) is calculated using Starburst99 models (Leitherer et al. 1999). The multiplicative mass-loading factor β accounts for unresolved molecular clouds. So total mass injected per timestep is

$$\dot{M} = \dot{M}_{\rm SN+SW} + \dot{M}_{\rm cold} = \beta \dot{M}_{\rm SN+SW}. \quad (4)$$

Evidently, this is a subset of that in CC85 because it does not include the diffuse ISM gas swept up by the wind. In my simulations the diffuse ISM is the initial density. Together ϵ and β determine outflow velocity as I explain in Section 2.2.

Some authors (Heckman et al. 2015; Muratov et al. 2015; Roberts-Borsani et al. 2020) use mass loading to refer exclusively to mass that leaves the galactic disk. This is a subset of the mass used in CC85 because only a fraction of the wind is directed out of the disk plane. That is, $\dot{M}_{\rm out}$ is only a fraction of $\dot{M}$ from Equation (4), but $\dot{M}_{\rm out}$ adds mass swept up from the ISM. However, $\dot{M} \propto \dot{M}_{\rm out}$ with proportionality that depends on the ambient ISM pressure and density, the extent and duration of the starburst, and the opening angle of the outflow. To establish the exact relation between $\dot{M}$ and $\dot{M}_{\rm out}$ would require simulations of starbursts on the sub-parsec scale with parameter studies of ambient ISM pressure and clumpiness, the effect of cosmic rays, and radiation pressure (Kim & Ostriker 2015; Schneider et al. 2020; Yu et al. 2020).

To avoid confusion I use β to refer to mass loading of the wind as defined in Equation (4), and

$$\eta = \frac{\dot{M}_{\rm out}}{\rm SFR} \quad (5)$$

to refer to mass loading from the galaxy, with $\dot{M}_{\rm out}$ the mass outflow rate. How η scales to other galaxy parameters is a common diagnostic of galactic wind properties (see the references in Rupke 2018).

Because β depends on $\dot{M}_{\rm cold}$—essentially a measure of the mass of the cloud not converted into stars—one can simply assume that β is inversely proportional to the star formation efficiency (SFE):

$$\beta \propto \frac{1}{\rm SFE}. \quad (6)$$

The exact relation would require higher-resolution simulations (e.g., Kim & Ostriker 2018; Hu 2019). This would imply that η is also inversely proportional to the SFE so both η and β can be proxies for the SFE.

2.2. Outflow Velocity

The simple model of CC85 assumes that thermal pressure on the ISM by a star cluster goes into the kinetic energy of the gas. This results in

$$v_A = v_0 \sqrt{2\frac{\epsilon}{\beta}} \quad (7)$$

which I refer to as the CC85 model velocity (for the derivation see Tanner17). Here I set $v_0 = 1894.0$ km s^{-1}; the exact value depends on the energy and mass injection, which I find using Starburst99 (Leitherer et al. 1999; Tanner17). Simulations from Tanner17 showed that the velocity of the hot wind does not depend on the SFR. This agress with Equation (7) because the SFR cancels out of the equation (Veilleux et al. 2005).

Tanner17 kept galaxy mass constant and varied the SFR. Here I keep SFR constant at 50 $M_\odot$ yr^{-1} but vary galaxy mass. CC85 assumed that gravity was not important for wind dynamics. But JA71 assumed that it was, so included gravitational potential energy. Based on their results, I start with

$$\frac{1}{2}\dot{M}v^2 = \dot{E} - \dot{M}\Delta\Phi(r) \quad (8)$$

with $\dot{E} = \epsilon \dot{E}_{\rm SN+SW}$ and $\dot{M} = \beta \dot{M}_{\rm SN+SW}$, where $\dot{E}_{\rm SN+SW}$ and $\dot{M}_{\rm SN+SW}$ are the contributions to the ISM from supernova and stellar winds and are linear functions of the SFR. Solving for velocity and simplifying results gives

$$v_G = \sqrt{2\left(v_0^2\frac{\epsilon}{\beta} - \Delta\Phi(r)\right)}, \quad (9)$$

which like Equation (7) does not depend on the SFR. I set v_A and ϵ and use Equation (7) to calculate β which determines the mass input at each simulation timestep. My values of v_A were chosen to span observed outflow velocities (Martin 2005;

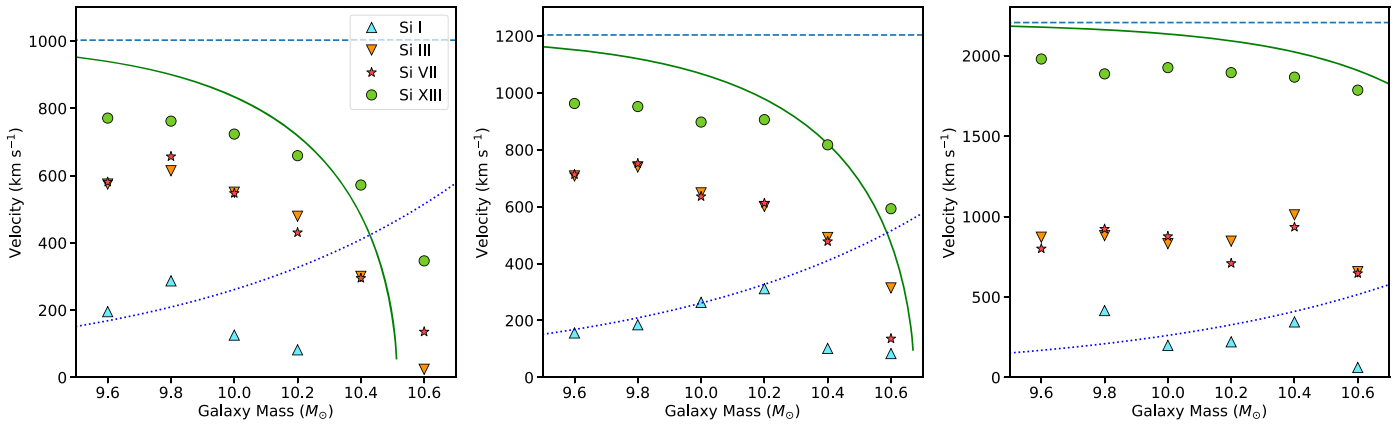

Figure 1. Plots of outflow velocity vs. galaxy mass. Outflow velocities are measured by Si I (upward triangles), Si III (downward triangles), Si VII (stars), and Si XIII (circles). CC85 model velocities of 1000 km s^{-1} (left), 1200 km s^{-1} (center), and 2200 km s^{-1} (right) are the horizontal dashed lines, corresponding to β of 7.2, 5.0, and 1.5, respectively. Each solid green curve indicates the JA71 model velocity, and dotted blue curve indicates the escape velocity for gas in the galactic nucleus.

Rupke et al. 2005; Chisholm et al. 2015, 2016). Note that some choices can yield nonphysical values of β, which will be addressed in Section 5. For now I compare measured outflow velocities to those predicted from Equations (7) and (9).

2.3. Simulation Velocities

I measure outflow velocities from synthetic absorption lines generated by the method in Tanner17. For simplicity I generate only silicon lines. I determine the outflow velocity of the multiphase gas from the Doppler shift of its line center ($v_{\rm cent}$), which is defined as the half width at half line depth. To remove possible contributions from stars or disk gas some authors use v_{90}, the velocity on the blueward side of the line where the absorption line reaches 90% of the adjacent continuum level. Both methods are used to measure outflow velocities (Martin 2005; Rupke et al. 2005; Weiner et al. 2009; Erb et al. 2012; Bordoloi et al. 2014; Chisholm et al. 2015, 2016; Heckman et al. 2015; Cicone et al. 2016; Ho et al. 2016; Heckman & Borthakur 2016; Martin et al. 2019). I use $v_{\rm cent}$ because it measures well the mass-weighted average velocity of the gas for a specific ionization state.

To trace the velocities of the cold, warm, and hot gas I tracked the Si I, Si III, Si VII, and Si XIII ions. As noted in Tanner17, the measured velocity increases with increasing ionization, with the biggest jumps between Si II and Si III, and Si XI and Si XII. Between Si III and Si X there is virtually no difference in the measured velocities.

3. Outflow Velocities

Tanner17 showed that the velocity of highly ionized gas ($v_{\rm hot}$) was ∼80%–90% of the CC85 model velocity and did not depend on the SFR. CC85 model velocities and mine differ because the CC85 model calculates the maximum velocity and I measure the velocity at line center, which provides an average velocity. Measurements of v_{90} are closer to the CC85 velocities, but both v_{90} and $v_{\rm cent}$ show similar trends (Tanner17). My simulations also cool the gas radiatively, but the cooling time for the hot gas is large compared to the simulation time, so has little effect.

Here I find that for a single value of β, $v_{\rm hot}$ decreases as expected with increasing galactic mass. While the difference between the original CC85 model and JA71 is small (<3%) for galaxies of mass $\leqslant 10^{9.6} M_\odot$, the predicted velocities diverge, sometimes significantly, for increasing galactic mass. Figure 1 shows the results of three sets of CC85 models spanning the galaxy masses tested. The CC85 velocities correspond to β of 7.2, 5.0, and 1.5 respectively. Each plots the outflow velocities predicted by the CC85 model (Equation (7)) and the JA71 model (Equation (9)). The velocities of the three gas phases, $v_{\rm hot}$, $v_{\rm warm}$, and $v_{\rm cold}$, are measured by Si XIII, Si VII or Si III, and Si I lines respectively. As noted in Section 2.3 and shown in Tanner17, there is no significant difference in velocities for ionization states III–X. This can be seen in the very similar measured velocities of Si III and Si VII in my simulations. Thus either ionization can be a proxy to measure the velocity of the warm phase.

Simulations with lower v_A, corresponding to higher values of β, show greater divergence between the CC85 and AJ71 predicted velocities. Lower-mass galaxies can outflow in all three phases. In higher-mass galaxies it is possible for β to quench the cold and warm phases so that the outflow is primarily hot gas, i.e., a galaxy whose SFE is such that the outflow is almost entirely hot X-ray-emitting gas with little optical or IR emission.

Both $v_{\rm hot}$ and $v_{\rm warm}$ follow the trend of the JA71 model, with $v_{\rm warm}$ lower than $v_{\rm hot}$. As explained in Tanner17, $v_{\rm warm}$ and $v_{\rm cold}$, unlike the hot gas, depend on the SFR such that increased SFR increases outflow velocities. But a higher SFR will only increase $v_{\rm warm}$ up to $\sim 0.8 v_{\rm hot}$, whereupon it saturates and is flat for increasing SFR. The saturation point for $v_{\rm cold}$ is $\sim 0.6 v_{\rm hot}$.

In the left and center panels of Figure 1, $v_{\rm warm}$ (measured by Si III and Si VII) has saturated so that, as $v_{\rm hot}$ decreases with increasing galaxy mass, $v_{\rm warm}$ decreases proportionally. In the right panel the warm gas is below the saturation point and appears to have the same slight downward trend as $v_{\rm hot}$, but the relation is less clear for simulations with similar CC85 model velocities. Figure A1 in the Appendix plots the velocities from all simulations. Below a CC85 model velocity of 1600 km s^{-1}, $v_{\rm warm}$ saturates and follows the same trend as $v_{\rm hot}$. The measured cold velocities vary much more because the cold gas in the wind clumps (Melioli et al. 2013), and ram pressure sets the velocity of each clump (Tanner17; Martin et al. 2019). But in simulations with low v_A and high β, the cold gas is entirely quenched for high-mass galaxies. Most $v_{\rm cold}$ measurements are below $v_{\rm escape}$, but because the velocities are measured at the line centers, some cold gas exceeds $v_{\rm escape}$.

Table 1
Slopes from Linear Fits to Outflow Mass versus Galaxy Mass (Figure 3)

Temperature Regime	Slope
Cold (<100 K)	−1.70
Hα (5000–40,000 K)	−0.97
Soft X-ray (0.5–3.0 keV)	−0.25
Mid X-ray (3.0–10.0 keV)	−0.24
Total mass	−0.85

4. Outflow Mass

To calculate the mass outflow rates in my simulations I measure the velocity vertical to the disk for each cell relative to the escape velocity ($v_{\rm out} = v_z - v_{\rm escape}$). For each simulation I make mass distributions by binning the mass of the cells according to $v_{\rm out}$ using $\Delta = 100\,{\rm km\,s^{-1}}$ bins, for all temperatures, and also for mass with the temperature ranges in Table 1. This gives the total mass outflow and those in different gas temperature ranges.

Figure 2 shows mass distributions of six representative models. As expected, higher v_A puts more mass at higher velocity, and a higher galaxy mass lowers total mass outflow for all temperature ranges. The majority of the outflow mass has temperatures in the soft X-ray (0.5–3 keV) and mid X-ray (3–10 keV) ranges. This counters the expectation that warm gas dominates the outflow mass, but the hot gas only dominates in galaxies with mass $>10^{9.6}M_\odot$. Below this the warm gas dominates the outflow mass; Figure 3 shows this crossover.

For each model I sum the total mass where $v > v_{\rm escape}$ and plot it in Figure 3. I fit the data using least-squares minimization and find a negative correlation between total outflow mass and galaxy mass with slope −0.85. Because constant mass is injected in my simulations, the total mass is directly proportional to the mass outflow rate. This allows direct comparison between the total outflow mass in my simulations and mass loading from a galaxy (η) as measured with the FIRE simulations of Muratov et al. (2015). Those authors found $\eta \propto v_{\rm cir}^{-1}$ for galaxies $>10^9 M_\odot$. From a set of galaxies with strong outflows Heckman et al. (2015) obtained an inverse correlation slope, −0.98. My measured slope is slightly less than either of these observations. But when I consider only the mass of the warm gas (5000–40,000 K) outflow, its slope, −0.97, agrees with their and other results (Creasey et al. 2013; Heckman et al. 2015; Muratov et al. 2015; McQuinn et al. 2019; Sugahara et al. 2019).

Figure 3 right plots the best fits for the total outflow mass and the outflow mass in the cold, warm, and hot phases (split into soft and mid X-ray temperature ranges). Both exhibit the same relation, but the mid X-ray range has ∼15× lower mass. Table 1 reports slopes for all relations. Evidently, the mass outflow of hot gas does not follow the correlations of warm or cold gas. Thus, emission from warm gas cannot be a proxy for the outflow mass of the hot gas, especially in higher-mass galaxies. Because the mass of soft X-ray-emitting gas dominates the outflow, estimates of the total mass outflow based on tracers of warm gas will significantly underestimate the total mass of the outflow in higher-mass galaxies, but is accurate in lower-mass galaxies.

Figure 4 plots the total mass of the outflow versus the ratio of ϵ and β. This ratio measures the general efficiency of the starburst, and determines the velocity of the outflow using Equation (9). The relationship between ϵ/β and the total mass of the outflow is nonlinear, peaking at $\epsilon/\beta = 0.2$–0.4. At these values the starburst is most efficient at removing gas from the galaxy. Assuming a fixed value for ϵ the ratio ϵ/β depends entirely on β. At lower β the gas velocity may be higher, but less mass loading reduces the density and therefore the wind mass. At higher β the wind may be denser, but moves more slowly so most gas will not escape the galaxy.

As noted in Section 2.1 for these simulations I fixed $\epsilon = 1.0$, but the thermalization efficiency can have a range of values between 0.01 and 1.0 with the possibility of changing over time. It is possible to get the same outflow velocity with different values of ϵ and β as long as the ratio is the same. This degeneracy prevents determining either ϵ or β from just kinematic measurements. But multiwavelength observations of outflows can be used to determine the total galactic outflow rate (η) from IR, optical, UV, and X-ray luminosities. When combined with simulations this can create a correlation between the measured luminosity of starbursts and the mass loading. This is currently an active area of research for the author.

5. Maximum Galaxy Mass for Outflows

Observations show a correlation between outflow velocity and circular velocity of the host galaxy (for example, Rupke et al. 2005; Heckman & Borthakur 2016) plotted in Figure 5 together with the outflow velocity as measured by Si III lines from my models; both observations yield similar least-squares fit slopes 0.90 and 0.77, respectively. Using the stellar mass set in each simulation and the Tully–Fischer relation in Reyes et al. (2011), Figure 5 also plots the circular velocity for each simulated galaxy using $v_{\rm cir} = 0.278 \log M_* - 0.666$.

As noted in Section 2.1 my simulations may have nonphysical ϵ and β values. Hence I cannot establish their values individually, but can constrain their ratio from Equations (7) and (9) by using the best fits from Heckman & Borthakur (2016) and Rupke et al. (2005). Physical values require (CC85) $\epsilon/\beta < 1.0$; anything above would require thermalization efficiency >1 and/or a mass loading <1, representing significant mass freeze-out from stellar winds and supernova. This becomes my cut-off point for starbursts that can form outflows. For both models, higher-mass galaxies must have correspondingly higher ϵ/β to fulfill the observed $v_{\rm max}$ versus $v_{\rm cir}$ relation. From the fits of Heckman & Borthakur (2016) and Rupke et al. (2005), the simple model of CC85 allows for possible outflows from galaxies $\lesssim 10^{13} M_\odot$. That CC85 has no intrinsic limit for outflows to form in galaxies with mass $>10^{12} M_\odot$ therefore requires another mechanism to quench outflows such as active galactic nuclei (AGNs) or depletion of disk gas.

Alternatively, the JA71 model cuts off just above $10^{11}\,M_\odot$; beyond, outflows require nonphysical values of ϵ and β. This allows starbursts to quench their own outflows in galaxies with mass $10^{11-12} M_\odot$ without invoking an AGN or gas depletion. Thus, the JA71 model yields $\approx 10^{11.5} M_\odot$ as the maximum allowable galaxy mass for outflows.

In Figure 5 the gray horizontal lines at constant $v_{\rm max}$ for all $v_{\rm cir}$ is constant ϵ/β from the CC85 model. The line for JA71 is identical for galaxies $<10^9 M_\odot$ but quickly diverges from CC85 for higher masses to produce the same maximum mass as Heckman & Borthakur and Rupke et al. for $\epsilon/\beta = 1.0$. The mass limit of Equation (9), being robust to a broad range of $v_{\rm max}$ versus $v_{\rm cir}$ slope fits, is not an artifact of galaxy selection.

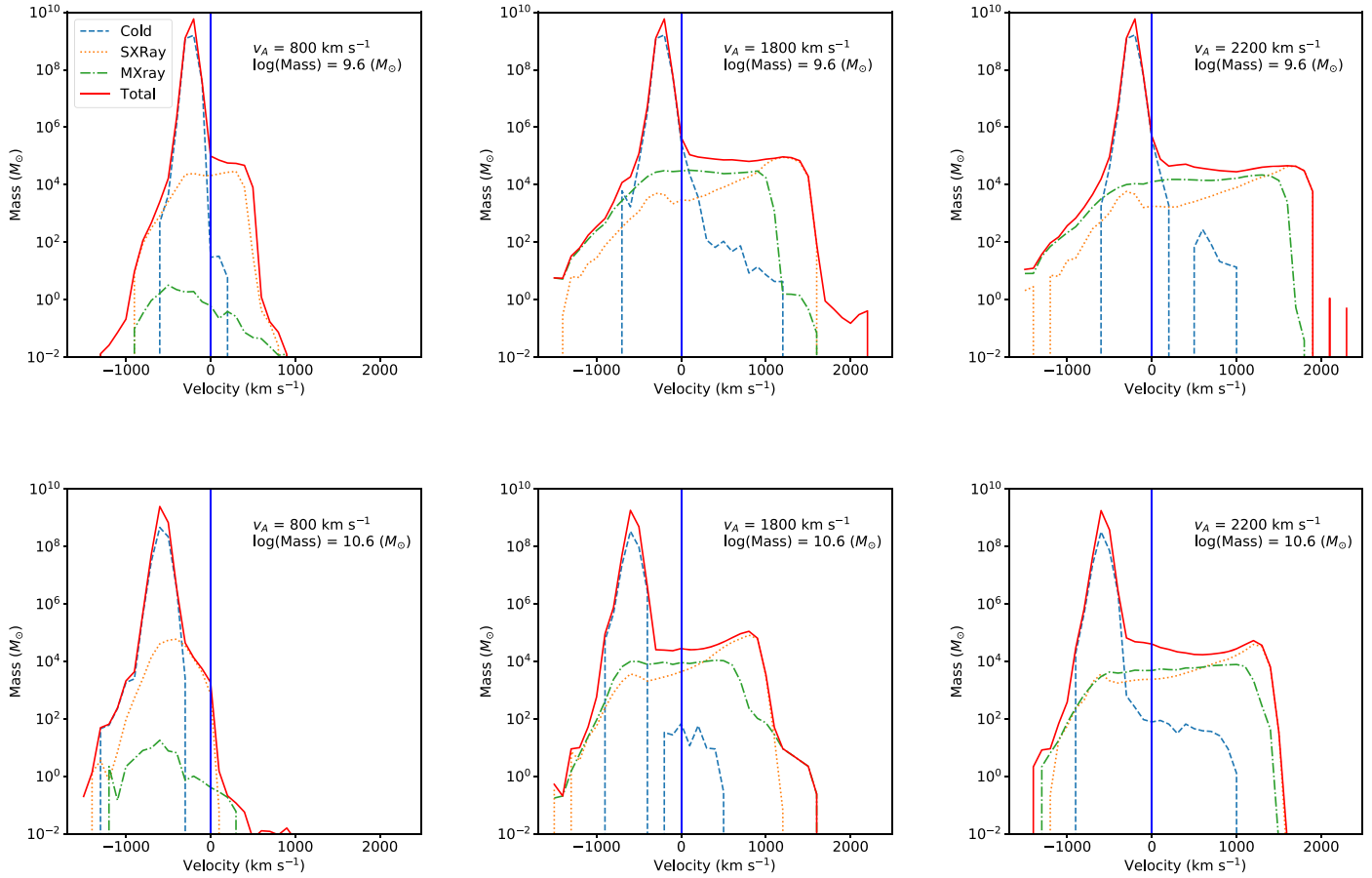

Figure 2. Example mass distributions binned according to $v_{\rm out}$ for two galaxy masses (top row $10^{9.6}\,M_\odot$, bottom $10^{10.6}\,M_\odot$) and CC85 model velocities 800, 1800, and 2200 km s^{-1} (left to right). $v = 0$ km s^{-1} $= v_{\rm escape}$ is the vertical blue line; gas to its left is bound by gravity, and to the right escapes. The solid red curves trace the total mass per velocity bin. The dotted orange curve and the dotted–dashed green curve show mass with temperatures in the soft X-ray and mid X-ray regimes respectively. The blue dashed curve shows cold mass at <100 K.

6. Discussion

6.1. Dynamics of a Three-phase Outflow

Tanner17 examined how the velocity of the three-phase outflow changes with the SFR. For a single galaxy mass $6 \times 10^9 M_\odot$ the CC85 model with radiative cooling sufficed to predict the velocity of the hot gas, but could only predict the velocities of warm and cold phases at a high SFR. In the present work with the SFR constant, I tested how the outflow velocity depends on the stellar mass of the galaxy, finding that the CC85 model is inadequate to describe the outflow velocity of hot gas for stellar mass $>10^{10} M_\odot$. The JA71 model—the CC85 model plus a gravitational potential—is needed to accurately model the velocity of the hot gas. This agrees with the analytic models of Yu et al. (2020), and disagrees with Schneider et al. (2020) who assumed that gravity does not affect that phase.

All recent hydrodynamical simulations include gravity, but analytic models that analyze model results often neglect it or assume it to be insignificant because an M82-mass galaxy is typically used (Cooper et al. 2008; Fujita et al. 2009; Creasey et al. 2013; Melioli et al. 2013; Roy et al. 2013; Sharma et al. 2014; Tanner et al. 2016, Tanner17; Schneider et al. 2020; Yu et al. 2020) where the difference between the CC85 and the JA71 models is small compared to other effects. However, my results show that for simulations with stellar mass $>10^{10} M_\odot$ gravity can dominate the dynamics of the hot gas, especially for higher-density (high-β) winds. Evidently, hydrodynamical simulations of outflows should not just assume an M82-mass galaxy, but also examine more massive galaxies.

For sufficiently high values of β the JA71 model also applies to the warm gas, but for $\beta < 3$ (corresponding to a hot wind speed of >1400 km s^{-1} and a warm wind speed of >900 km s^{-1}) it does not appear that the JA71 model adequately describes the dynamics of the warm phase. Recent approaches model neutral or slightly ionized gas as clouds driven by ram pressure (Heckman et al. 2015; Martin et al. 2019) rather than a gas shell driven by the starburst as CC85 and JA71 assumed. The cloud+ram pressure model has successfully explained observations of cold, dense clouds in a hot wind (Cooper et al. 2009; Tanner et al. 2016) that ablate mass to contribute to the warm phase. However, simulations have also shown that ram pressure will disrupt clouds, so cannot account for the mass of warm gas observed in the winds (Brüggen & Scannapieco 2016; Schneider & Robertson 2017; Zhang et al. 2017; Schneider et al. 2020). This discrepancy highlights the need for simulations having different wind geometry and refined physics.

Finally, my results show in Figures 1 and A1 that the gas outflow has three distinct phases with different velocities. Factors that set each phase include mass loading (β), gravity, SFR, and wind geometry. For example, β sets the outflow velocities of all three phases, the SFR only affects the warm and cold phases, while gravity has biggest effect on the hot

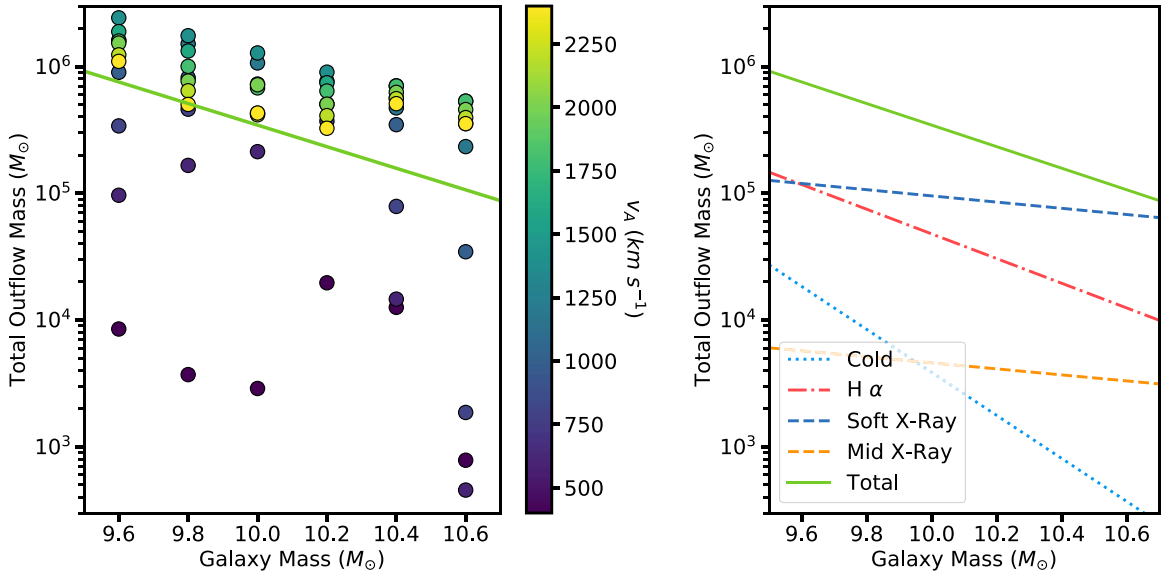

Figure 3. Left: total mass above the escape velocity (everything to the right of the vertical lines in Figure 2) with respect to galactic mass. All 66 simulations are plotted, and each dot is colored according to the CC85 model velocity. In solid green is the linear fit to the data with slope −0.85. Right: total mass in various gas temperature regimes from my simulations and their linear fits (fitted slopes given in Table 1).

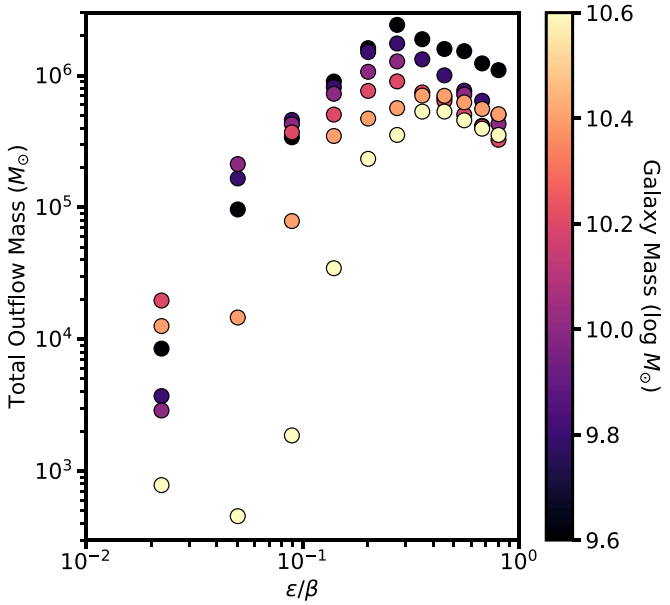

Figure 4. Same total masses from Figure 3 plotted with respect to ϵ/β of each simulation using Equation (7). The outflow velocity for the simulations increases from left to right. Circle coloring indicates the galactic mass for each simulation.

phase. Each phase should be considered separately with its own analytic model as done recently (Heckman et al. 2015; Martin et al. 2019; Schneider et al. 2020).

The values of β that I have worked with here should be considered as upper limits. Because I set $\epsilon = 1.0$, more realistic values of ϵ would require lower values of β to produce the same hot gas velocity. As β has a lower limit of 1.0, the value of ϵ will determine the upper limit for the hot gas velocity from starburst-driven winds.

6.2. Outflow Mass

When considering simulations with the same mass loading, more massive galaxies have less total mass outflow than less massive galaxies because of their deeper gravitational potential. The correlation of total outflow mass versus galaxy mass that I find has a shallower slope than that observed, and in other simulations (Creasey et al. 2013; Heckman et al. 2015; Muratov et al. 2015). But summing only the gas mass at peak Hα emission (5000–40,000 K) matched the observed slope ≈ -1.

This correlation is used in subgrid models of cosmological simulations (Springel & Hernquist 2003; Agertz et al. 2013; Muratov et al. 2015; Pillepich et al. 2018; Huang et al. 2020). But as Figure 3 shows, its slope only holds for the warm phase. The slope of the hot phase is much shallower, ≈ -0.25. Thus not only are their velocities potentially quite different between warm and hot phases (Section 3), but galactic mass loading and gas mass differ for the warm and hot phases. For galaxies with $>10^{10} M_\odot$ the hot gas dominates the outflow mass, becoming by $\sim 10^{11} M_\odot$ $\sim 10\times$ more massive than the warm phase. Thus the hot and warm gas outflows should be considered separately in the sub-grid models of cosmological simulations. Moreover, a negative correlation, -1, was established using Hα tracers and similar optical/UV emission. The correlation for the hot X-ray-emitting gas should be confirmed through similar X-ray measurements.

In this paper I focus solely on the slope or relationship between the total outflow mass and stellar mass. The actual amount of mass flowing out of the galaxy would depend on the SFR, ϵ, β, and the ambient pressure. As shown in Figure 4 the outflow mass is maximized for a certain range of ϵ/β. Because multiple values of ϵ and β can produce the same value for ϵ/β, further work will be needed to disentangle this degeneracy. But a lower value of ϵ will require a corresponding lower value of β to achieve the same wind velocity. This will decrease the total mass in the outflow.

While I have fixed the SFR at 50 $M_\odot$ yr^{-1}, a higher or lower SFR will raise or lower the total mass in the wind. The exact relation between the mass outflow and the SFR would have to be considered for each of the three gas phases separately. The hot gas mass should have a direct relation to the SFR, but the outflow mass in warm and cold phases will have a much more

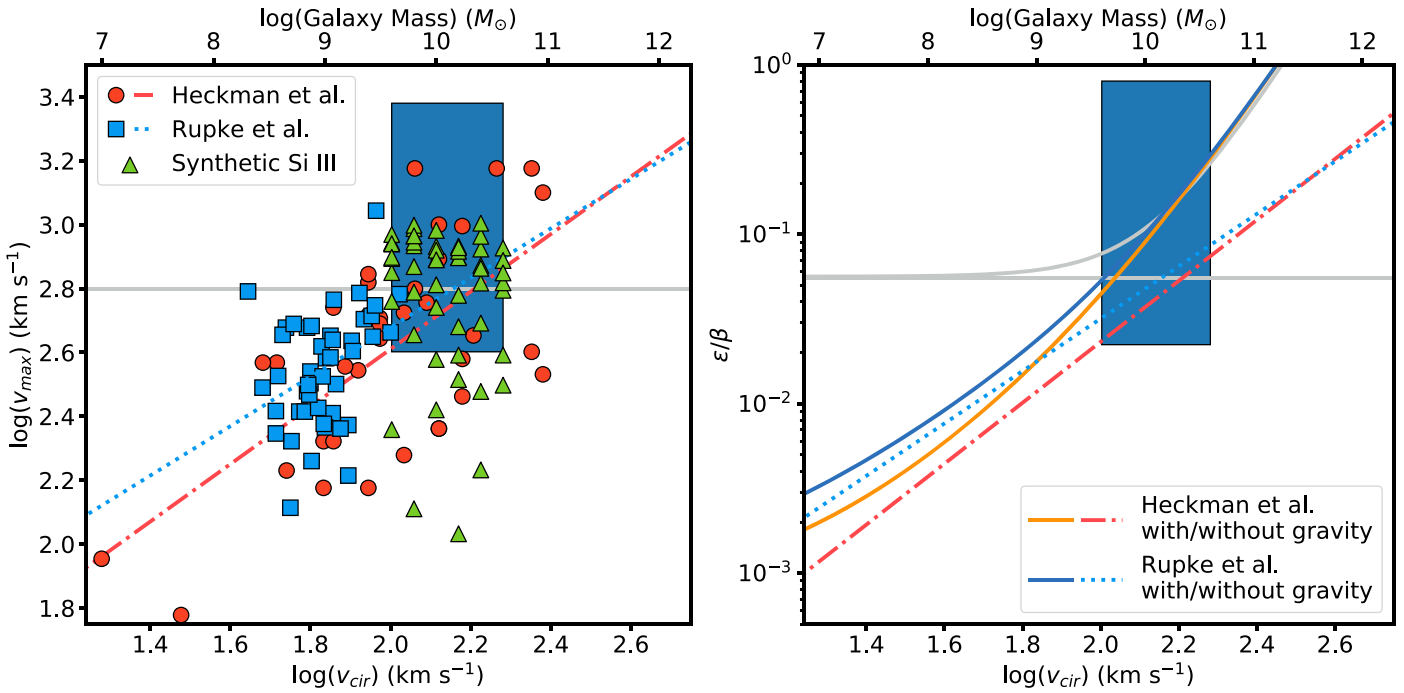

Figure 5. Left: maximum outflow velocity vs. circular velocity. Red circles are data from Heckman & Borthakur (2016); blue squares are data from Rupke et al. (2005). Lines show fits for both data sets. Green triangles show velocities from my simulations of the Si III lines. In both panels the blue rectangle shows the parameter space of my simulations. I have included a fit (gray line) at a constant v_{max} for all v_{cir}. In the CC85 model this corresponds to constant ϵ/β. Right: best fits of Heckman & Borthakur and Rupke et al. converted into ϵ/β values using the JA71 and CC85 models (with and without gravity). The two gray lines show ϵ/β for the constant v_{max} as computed using the JA71 and CC85 models.

complex relation but should also increase with increasing SFR. This would also need further study.

6.3. Limiting Efficiencies

As explained in Section 2.1 some values of ϵ and β that I chose can be nonphysical. Observations (Rupke et al. 2005; Heckman & Borthakur 2016) show that outflow velocity increases with galaxy mass. In contrast, results in Section 3 show that the outflow velocity should decrease with increasing galaxy mass. This decrease only occurs at constant ϵ and β, but their values can evolve over time so ϵ/β can vary with galaxy mass. Given the fits from Heckman & Borthakur (2016) and Rupke et al. (2005) in Figure 5, when calculating ϵ/β using Equations (7) and (9), ϵ/β clearly increases with galaxy mass. Thus thermalization efficiency would be higher and/or the mass loading would be lower in higher-mass galaxies. This represents a fundamental shift in thinking about starburst efficiencies in galaxies of different mass.

For ϵ/β to increase either ϵ must increase or β must decrease, or both. For the highest-mass galaxies the values of ϵ and β must converge to 1.0 to maintain an outflow. This would require that all radiation from the starburst be absorbed by the ISM, and that the SFE be as high as possible. Physical limitations of the thermalization and star formation efficiencies will set an upper stellar mass limit at which galaxies can form outflows.

The CC85 model shows that ϵ/β must increase linearly to increase velocity as galactic mass increases. However, the divergence of the JA71 model from the CC85 model at $>10^{10} M_\odot$ shows that the fits from Heckman & Borthakur (2016) and Rupke et al. (2005) would require unrealistic values of the thermalization efficiency and mass loading for galaxies $>10^{11.5} M_\odot$. Because the data scatter, it would be possible to have outflows with a galaxy mass $>10^{11.5} M_\odot$, but by $10^{12} M_\odot$ all outflows should be quenched from the limit on starburst efficiency.

This result explains the scarcity of outflows in galaxies of $>10^{11} M_\odot$, where outflow would require no loss of radiative energy and minimal mass loading into the wind beyond that from supernova ejecta and stellar winds. How adding cosmic rays, radiation pressure, magnetic fields, and other effects would influence this mass limit must be investigated. But application of the JA71 model shows that starburst-driven galactic outflows will quench somewhere between 10^{11} and $10^{12} M_\odot$ even without an AGN. This only explains quenching of outflows and not of star formation, although it is possible that the mechanisms that increase ϵ/β in high-mass galaxies also quench star formation. While AGNs certainly have a critical role in regulating outflows, the JA71 model suggests that starburst-driven outflows can self-regulate.

7. Conclusions

1. The model of CC85 for outflows is accurate for low-mass galaxies, but the gravity at higher masses greatly affects outflow kinematics. Analytic models of outflows with $>10^{10} M_\odot$ must include gravity. The JA71 model should be used for galaxies more massive than M82 (or equivalent Yu et al. 2020) to estimate the kinematics of hot gas but not necessarily those of outflowing warm and cold gas.
2. Outflow kinematics differ for each of the three phases, so should be considered separately in analytic models.
3. Using M82 as the canonical model in many 3D hydrodynamical simulations undervalues the influence of gravity when comparing simulations to analytic models and observations. Either a higher-mass galaxy

like NGC 3079 should be used, or a mix of high- and low-mass galaxies.
4. The mass outflow, or galactic mass loading, versus galaxy mass relation differs for different gas phases. The hot gas has a relatively shallow relation, the warm gas steeper, and cold gas even steeper. Thus outflows from high-mass galaxies are almost entirely of hot gas.
5. Different dynamics of the three phases emphasizes the need for multi-wavelength observations. Properties of neutral or slightly ionized gas are not necessarily relevant to those of highly ionized gas.
6. When interpreting observational fits, the JA71 model yields physically realistic values of thermalization efficiency and mass loading of outflows up to galaxy mass $\sim 10^{11.5} M_{\odot}$, independent of the SFR. Above this, outflows are prohibited by the excessive efficiencies required of the starburst.

I acknowledge the support of Gerald Cecil and his comments that improved this paper. My code and analysis methods were developed with support through our NASA Herschel grant NHSC-OT-1-1436036 (P.I. S. Veilleux). I also acknowledge Tom Crute at Augusta University and Kim Weaver of GSFC for support and encouragement.

Appendix
Outflow Velocities

In Figure A1 I include the outflow velocities for all of my simulations along with analytic calculations of the velocities based on CC85 and JA71.

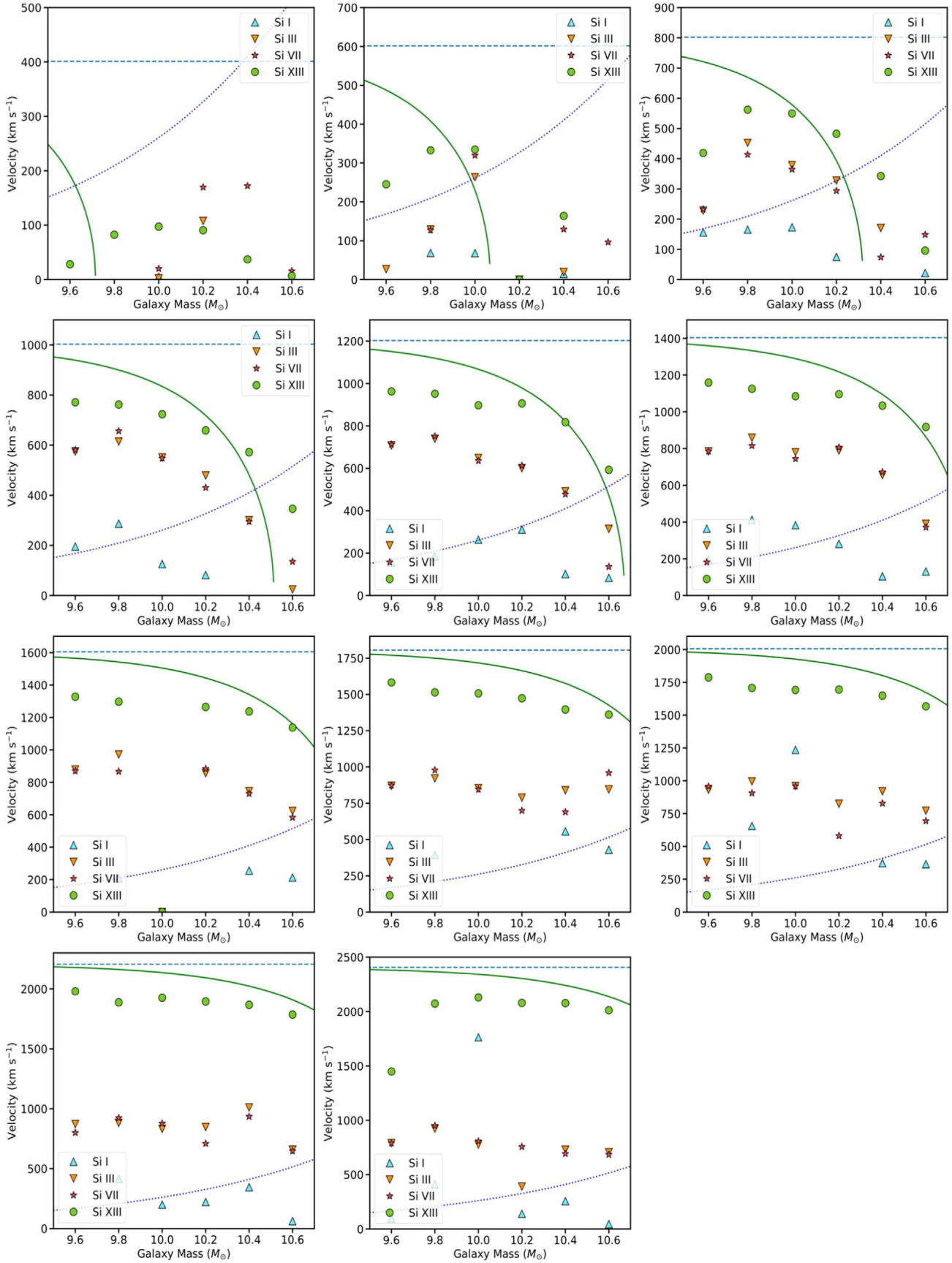

Figure A1. As for Figure 1: outflow velocity vs. galaxy mass. Outflow velocities are measured by Si I (upward triangles), Si III (downward triangles), Si VII (stars), and Si XIII (circles). In each panel the blue dashed line indicates the CC85 model velocity ranging from 400 km s^{-1} (top left) to 2400 km s^{-1} (bottom center). The solid green curve is the CC85 model velocity modified to include the gravitational potential, and the dotted purple curve is the escape velocity for gas in the galactic nucleus.

ORCID iDs

Ryan Tanner https://orcid.org/0000-0002-1359-1626

References

Agertz, O., Kravtsov, A. V., Leitner, S. N., & Gnedin, N. Y. 2013, ApJ, 770, 25
Bordoloi, R., Lilly, S. J., Hardmeier, E., et al. 2014, ApJ, 794, 130
Brüggen, M., & Scannapieco, E. 2016, ApJ, 822, 31
Chevalier, R. A., & Clegg, A. W. 1985, Natur, 317, 44
Chisholm, J., Tremonti, C. A., Leitherer, C., et al. 2015, ApJ, 811, 149
Chisholm, J., Tremonti, C. A., Leitherer, C., Chen, Y., & Wofford, A. 2016, MNRAS, 457, 3133
Cicone, C., Maiolino, R., & Marconi, A. 2016, A&A, 588, A41
Cooper, J. L., Bicknell, G. V., Sutherland, R. S., & Bland-Hawthorn, J. 2008, ApJ, 674, 157
Cooper, J. L., Bicknell, G. V., Sutherland, R. S., & Bland-Hawthorn, J. 2009, ApJ, 703, 330
Creasey, P., Theuns, T., & Bower, R. G. 2013, MNRAS, 429, 1922
Erb, D. K., Quider, A. M., Henry, A. L., & Martin, C. L. 2012, ApJ, 759, 26
Freyer, T., Hensler, G., & Yorke, H. W. 2003, ApJ, 594, 888
Fujita, A., Martin, C. L., Mac Low, M.-M., New, K. C. B., & Weaver, R. 2009, ApJ, 698, 693
Heckman, T. M., Alexandroff, R. M., Borthakur, S., Overzier, R., & Leitherer, C. 2015, ApJ, 809, 147
Heckman, T. M., & Borthakur, S. 2016, ApJ, 822, 9
Heckman, T. M., & Thompson, T. A. 2017, Galactic Winds and the Role Played by Massive Stars, in Handbook of Supernovae, ed. A. W. Alsabti & P. Murdin (Berlin: Springer), 2431
Ho, I.-T., Medling, A. M., Bland-Hawthorn, J., et al. 2016, MNRAS, 457, 1257
Hopkins, P. F., Chan, T. K., Garrison-Kimmel, S., et al. 2020, MNRAS, 492, 3465
Hu, C.-Y. 2019, MNRAS, 483, 3363
Huang, S., Katz, N., Davé, R., et al. 2020, MNRAS, 493, 1
Ipavich, F. M. 1975, ApJ, 196, 107
Johnson, H. E., & Axford, W. I. 1971, ApJ, 165, 381
Kim, C.-G., & Ostriker, E. C. 2015, ApJ, 802, 99
Kim, C.-G., & Ostriker, E. C. 2018, ApJ, 853, 173
Lehnert, M. D., Heckman, T. M., & Weaver, K. A. 1999, ApJ, 523, 575
Leitherer, C., Schaerer, D., Goldader, J. D., et al. 1999, ApJS, 123, 3
Martin, C. L. 2005, ApJ, 621, 227
Martin, C. L., Ho, S. H., Kacprzak, G. G., & Churchill, C. W. 2019, ApJ, 878, 84
McCormick, A., Veilleux, S., & Rupke, D. S. N. 2013, ApJ, 774, 126
McQuinn, K. B. W., van Zee, L., & Skillman, E. D. 2019, ApJ, 886, 74
Melioli, C., de Gouveia Dal Pino, E. M., & Geraissate, F. G. 2013, MNRAS, 430, 3235
Miyamoto, M., & Nagai, R. 1975, PASJ, 27, 533
Muratov, A. L., Kereš, D., Faucher-Giguère, C.-A., et al. 2015, MNRAS, 454, 2691
Nath, B. B., & Silk, J. 2009, MNRAS, 396, L90
Pillepich, A., Springel, V., Nelson, D., et al. 2018, MNRAS, 473, 4077
Reyes, R., Mandelbaum, R., Gunn, J. E., Pizagno, J., & Lackner, C. N. 2011, MNRAS, 417, 2347
Roberts-Borsani, G. W., Saintonge, A., Masters, K. L., & Stark, D. V. 2020, MNRAS, 493, 3081
Roy, A., Nath, B. B., Sharma, P., & Shchekinov, Y. 2013, MNRAS, 434, 3572
Rupke, D. 2018, Galax, 6, 138
Rupke, D. S., Veilleux, S., & Sanders, D. B. 2005, ApJS, 160, 115
Schneider, E. E., Ostriker, E. C., Robertson, B. E., & Thompson, T. A. 2020, ApJ, 895, 43
Schneider, E. E., & Robertson, B. E. 2017, ApJ, 834, 144
Sharma, M., Nath, B. B., Chattopadhyay, I., & Shchekinov, Y. 2014, MNRAS, 441, 431
Silich, S., Tenorio-Tagle, G., Torres-Campos, A., et al. 2009, ApJ, 700, 931
Springel, V., & Hernquist, L. 2003, MNRAS, 339, 312
Stone, J. M., Gardiner, T. A., Teuben, P., Hawley, J. F., & Simon, J. B. 2008, ApJS, 178, 137
Strickland, D. K., & Heckman, T. M. 2009, ApJ, 697, 2030
Strickland, D. K., & Stevens, I. R. 2000, MNRAS, 314, 511
Sugahara, Y., Ouchi, M., Harikane, Y., et al. 2019, ApJ, 886, 29
Tanner, R., Cecil, G., & Heitsch, F. 2016, ApJ, 821, 7
Tanner, R., Cecil, G., & Heitsch, F. 2017, ApJ, 843, 137
Thompson, T. A., Fabian, A. C., Quataert, E., & Murray, N. 2015, MNRAS, 449, 147
Veilleux, S., Cecil, G., & Bland-Hawthorn, J. 2005, ARA&A, 43, 769
Veilleux, S., Maiolino, R., Bolatto, A. D., & Aalto, S. 2020, A&ARv, 28, 2
Veilleux, S., Rupke, D. S. N., & Swaters, R. 2009, ApJL, 700, L149
Weiner, B. J., Coil, A. L., Prochaska, J. X., et al. 2009, ApJ, 692, 187
Yu, B. P. B., Owen, E. R., Wu, K., & Ferreras, I. 2020, MNRAS, 492, 3179
Zhang, D., Davis, S. W., Jiang, Y.-F., & Stone, J. M. 2018, ApJ, 854, 110
Zhang, D., Thompson, T. A., Quataert, E., & Murray, N. 2017, MNRAS, 468, 4801